Title

Enhanced Water Management of Polymer Electrolyte Fuel Cells with Additive-Containing Microporous Layers

Journal

ACS Applied Energy Materials, 1(11)

ISSN

2574-0962

Authors

Spernjak, Dusan
Mukundan, Rangachary
Borup, Rodney L
et al.

Publication Date

2018-11-26

DOI

10.1021/acsaem.8b01059

Enhanced Water Management of Polymer Electrolyte Fuel Cells with Additive-Containing Microporous Layers

Dusan Spernjak[1,+], Rangachary Mukundan[1,+], Rodney L. Borup[1,+], Liam G. Connolly[2], Benjamin I. Zackin[2], Vincent De Andrade[4], Michael Wojcik[4], Dilworth Y. Parkinson[5], David L. Jacobson[7], Daniel S. Hussey[7], Karren L. More[8], Thomas Chan[6], Adam Z. Weber[6], Iryna V. Zenyuk[2,3]*

[1]Los Alamos National Laboratory (LANL), MS D429, Los Alamos, New Mexico, 87545
[2]Department of Mechanical Engineering, Tufts University, Medford, MA 02155
[3]Department of Chemical Engineering and Materials Science; National Fuel Cells Research Center, University of California, Irvine, CA 92617
[4]Advanced Photon Source, Argonne National Laboratory, Argonne, IL 60439, USA

[5]Advanced Light Source,
[6]Energy Technologies Area, Lawrence Berkeley National Laboratory, 1 Cyclotron Road, Berkeley CA 94720, USA

[7]National Institute of Standards and Technology, 100 Bureau Drive, MS 846, Gaithersburg, MD 20899, USA

[8]Center for Nanophase Materials Sciences, Oak Ridge National Laboratory, 1 Bethel Valley Road, Oak Ridge, TN 37831-6064, USA

*Corresponding author: I.V.Zenyuk (e-mail: Iryna.zenyuk@uci.edu)

[+]The authors contributed equivalently

Keywords: fuel cells, microporous layer, water management, transport phenomena, material design

Abstract

This work describes the performance improvement of a polymer electrolyte fuel cell with a novel class of microporous layers (MPLs) that incorporates hydrophilic additives: one with 30 μm aluminosilicate fibers and the other with multiwalled carbon nanotubes with a domain size of 5 μm. Higher current densities at low potentials were observed for cells with the additive-containing MPLs compared to a baseline cell with a conventional MPL, which correlate with improvements in water management. This is also observed for the helium/oxygen experiments and by the lower amount of liquid water in the cell as determined by neutron radiography. Furthermore, the carbon-

nanotube-containing MPL demonstrates improved durability compared to the baseline MPL. Microstructural analyses including nanotomography demonstrate that the filler material in both the additive-containing MPLs provide preferential transport pathways for liquid water, which correlate with *ex-situ* measurements. The main advantage provided by these MPLs is improved liquid-water removal from the cathode catalyst layer resulting in enhanced oxygen delivery to the electrocatalyst sites.

1. Introduction

Polymer-electrolyte fuel cells (PEFCs) are promising zero-emission electrochemical energy-conversion systems that use hydrogen as a fuel [1-2]. Since PEFCs operate at relatively low temperatures (80°C or lower), water management becomes an important consideration, especially during colder operation and startup [3-6]. Water is produced as a byproduct of the oxygen reduction reaction (ORR) in the cathode catalyst layer (CCL) and must be efficiently removed into the gas channel in order to not flood and impede reactant flow in the thin CCL. Water is needed to humidify the membrane, as its ionic conductivity strongly depends on its hydration [7]. For water management, the CCL is pressed against a hydrophobic microporous layer (MPL) composed of carbon black and polytetrafluoroethylene (PTFE). The MPL is integrated with a gas-diffusion layer (GDL) backing, which consists of carbon fibers coated with PTFE [8]. This MPL provides good contact between the more macroporous GDL and the microporous CL. Furthermore, in terms of water management, the purpose of the ~50 μm thick MPL is to ensure sufficient hydration level in the membrane and ionomer in the CL [9-10] [11]. Small and hydrophobic MPL pores ensure gas pathway (due to higher saturated vapor pressure, per the Kelvin equation). The MPL also acts as a higher capillary barrier for water removal from the CCL into cathode channel [12] [13] . This barrier is beneficial to maintaining high hydration of the CCL, however it can be damaging to the

performance when the CCL hydration is excessive (flooding). Another MPL effect is enhanced water removal via an evaporative mechanism (i.e., phase-change-induced flow) due to the MPL's inherently low thermal conductivity, as larger thermal gradients can build up due to the heat-generation in the CCL[3, 5, 14-16]. In general, studies have shown that a 20 to 30% performance increase can be achieved for PEFCs that incorporate an MPL [17-18]. Furthermore, improved water management with MPL incorporation can be beneficial to durability [19].

In recent years, many researchers have explored the effects of the MPL wettability and microstructure on water management, and novel MPL design concepts have emerged [20-30]. Doping the MPL with various nanomaterials has proved to be an effective way to improve water management and increase potentials at high current-density operation, although the exact mechanism(s) for water removal and the concomitant increased performance are not well understood [31-39]. Many of these dopants are hydrophilic in nature, which questions the convention of having a hydrophobic MPL interfaced with the cathode. In fact, Weber predicted in a modeling study that the addition of hydrophilic pathways through an MPL could help increase performance by providing hydraulic conductivity between the catalyst layer and GDL, thus enabling more efficient water removal [40]. One should note that while water-filled cracks may provide such hydrophilic connections, they are also typically large and can result in reactant maldistributions, as well as being a durability concern [10, 41-42]. Zhou et al. found that optimal content of hydrophilic material within MPL is somewhere between 10 to 20 % and predicted that hydrophilic domains increase overall surface area of water front enhancing water evaporation and removal from the CL[20].

Among the additives considered for MPLs are multiwalled carbon nanotubes (MWCNTs). Lee et al. [37] used *operando* X-ray radiography to probe the water content of cells with conventional MPLs

and MPLs containing MWCNTs (SGL 25 BN[43]). The SGL 25 BN cell exhibited a performance increase at high current density, which was attributed it to higher MPL porosity and improved oxygen transport. Gharibi et al. [44] also demonstrated an increase in the performance of the cell with MWCNTs, which was attributed primarily to the increased oxygen diffusion and possibly increased electrical resistance, results which were confirmed by Schweiss et al. [24, 31]

The works mentioned above focused primarily on understanding reactant delivery to the CCL and the role of hydrophilic MPLs in gas transport. In the present work, we use novel characterization techniques to probe the morphology and water distribution systematically within cells incorporating three types of MPLs: 1) a conventional hydrophobic SGL 25 BC, 2) a SGL 25 BN with MWCTN domains, and 3) a SGL 25 BL that contains aluminosilicate fibers. Our earlier work focused on SGL 25 BL, where the polarization behavior and impedance were correlated with neutron imaging of water and the benefit of hydrophilic pathways created by the aluminosilicate fiber additive in transporting generated liquid water away from the CCL [26]. Here, we use electrochemical polarization behavior with electrochemical impedance spectroscopy (EIS), along with both *ex situ* and *in situ* X-ray micro- and nano- computed tomography (CT), *operando* neutron radiography, and other characterization techniques to explain the performance changes observed for PEFCs with two additive-containing MPLs.

2. Materials and Methods

2.1. Materials

All GDL materials (from SGL Technologies GmbH) had identical graphitized carbon-fiber substrate with 5% PTFE (which is essentially the GDL material SGL 25 BA which does not contain any MPL). The baseline GDL with MPL is SGL24BC, which has the carbon-fiber substrate identical to SGL25BA, but with an MPL containing 23% PTFE. The two GDL materials with additive-containing MPLs were

fabricated as follows. The SGL 25 BL was prepared by mixing 10 wt.% aluminosilicate fibers into the carbon black PTFE paste followed by a heat treatment at 350 °C. The SGL 25 BN MPL was prepared by mixing 21 wt.% MWCNTs, 15 wt.% PTFE, and 64 wt.% carbon black. This particular ratio of carbon black to MWCNTs was chosen for practical reasons, as it is a tradeoff between the CNT content and the ink viscosity. Performance variation with CNT content is reported in Ref. [31]. The material properties of the GDL and MPLs are given in Table 1. The additive domain sizes and volume fractions within the MPL are obtained via X-ray CT. Table 1 also shows an abbreviations for these materials as will be used subsequently in the manuscript.

Table 1. Basic properties and composition of the four GDL and MPL materials.

Properties	SGL 25 BA	SGL 25 BC	SGL 25 BL	SGL 25 BN
Abbreviation	BA	BC	BL	BN
Thickness	190 µm	(235 ± 20) µm	230 µm	228 µm
PTFE content in the carbon-fiber substrate (wt %)	5	5	5	5
MPL composition (wt %)	-	77 wt.% carbon 23 wt.% PTFE	67 wt.% carbon, 10 wt.% alumosilicate fibers, 23 wt.% PTFE	64 wt.% carbon, 15 wt.% PTFE, 21 wt.% MWCNTs
Additive domain sizes (µm) and volume fraction	-	-	(29 ± 8.7) µm 2.1 % volume	~5 µm 40 % volume
Pore diameter in MPL (µm), only micropores	-	0.08 [37]	0.09 [26]	0.08 [37]

2.2.Fuel-cell testing

PEFCs were assembled using SGL 24 BC on the anode and BC, BL, or BN on the cathode. Gore Primea membrane electrode assemblies (MEAs) (A510.2/M710.18/C510.4) were used, with Pt loading of 0.2 mg_{Pt} cm^{-2} and 0.4 mg_{Pt} cm^{-2} on anode and cathode, respectively, and 18 µm thick 710-type membrane. Fuel cell testing was performed in a 50 cm^2 Fuel Cell Technologies (FCT) quad-serpentine hardware unless otherwise stated. The fuel cell performance and characterization

were performed in a co-flow configuration (inlets high) with the FCT test station. Polarization curves were recorded with both decreasing and increasing voltage (averages reported). The baseline operating conditions were 80°C, 100% RH, 1.2/2 stoichiometry of H_2/air, and 275 kPa backpressure. To quantify mass transport, measurements in HelOx (21% O_2, balance Helium) were conducted in addition to EIS at various current densities. The EIS data were fit with a simple equivalent circuit as described by Arisetty et al.[45] and Spernjak et al. [42]

Ex situ and *in situ* durability tests were performed on the BC GDL. The *ex situ* ageing was performed using an accelerated test developed under the DECODE project [46], which consisted of boiling in a 30 % H_2O_2 solution at 95 °C for up to 15 hr [47]. The *in situ* durability testing was performed using a portion of the USDRIVE Fuel cell Tech Team (FCTT) durability protocol [48], which consisted of cycling between 0.02 A cm^{-2} (30 s) and 1.2 A cm^{-2} (30 s) at 80 °C, 113 % RH and 101.3 kPa.

2.3.Neutron Radiography

Neutron imaging was performed at the NIST Center for Neutron Research (NCNR) on thermal beam tube 2 [49-50]. The measurements were performed using a 1 cm tall by 1 mm wide slit providing a corresponding collimation ratio of 600,6000 (height and width) with a neutron fluence rate of 6×10^5 cm^{-2} s^{-1}. The imaging was performed using a 40 mm diameter cross-strip microchannel plate detector with a spatial resolution of about 15 µm [51]. The PEFCs were tested in hardware with an active area of 2.5 cm^2 as described elsewhere [52] using the same MEAs as the fuel cell testing. The testing conditions at NIST were 80 °C, 100 % RH, 100 sccm/200 sccm of H_2/air on the anode and cathode, respectively (fixed flow rates, in standard cubic centimeters), with zero applied backpressure. EIS was collected *in situ* using a PARSTAT 2273 potentiostat/galvanostat at constant current densities. Water profiles reported herein are 20-minute averages over entire cell

area, obtained at a constant current after cell has operated at same condition for 25 minutes. EIS was recorded after the 45-minute operation at constant conditions. More details about the high-resolution neutron imaging, cell hardware, and image processing can be found elsewhere [49, 53]. In addition, polarization curves were collected while decreasing potential from 1.0 V to 0.3 V and back to 1.0 V, in 50 mV voltage-control steps where duration of each voltage step was 1 minute. For these small neutron imaging cells, we report the average polarization curve of decreasing/increasing voltage.

2.4. X-ray computed tomography

Micro X-ray CT and image processing

Micro X-ray computed tomography was performed at Beamline 8.3.2 at the Advanced Light Source (ALS) at Lawrence Berkeley National Laboratory. A double-multilayer monochromator was used to select 20 keV X-rays, and detection was performed with a 0.5 mm LuAG scintillator and 5x lenses with a sCMOS PCO Edge camera, giving a 1.3 μm pixel dimension, and a 3.3 mm horizontal field of view (FOV). For each tomographic scan, 1025 projections were acquired over a 180° rotation with a 300 ms exposure time. Image reconstructions of the acquired back-projections were performed using a Modified Bronnikov Algorithm (MBA), which is part of the open-source ImageJ/Fiji [54-55] software coupled to Octopus 8.5 [56].

Nano X-ray CT and image processing

Nano X-ray CT imaging was performed at the Advanced Photon Sources (APS) at Argonne National Laboratory (ANL) using Beamline 32-ID. Monochromatic X-rays illuminate the beam shaping condenser, pass through the sample, a Fresnel zone plate (FZ), and are collected by an imaging detector. The sample is placed on the tip of a metal pin, which is fixed onto a rotary stage

that rotates 180° enabling three-dimensional reconstruction. FZ plates with grating of 60 nm were used to achieve resolution of 60 nm. The FOV was 75 µm x 75 µm and the scan-time was approximately 20 min. with 1 s per projection with 1500 projections recorded. Zernike phase contrast was used to detect low atomic mass elements such as carbon. Hutch RH was measured to be 50 %. For experiments with water, a water droplet was added after two preliminary dry scans.

Image phase retrieval and reconstructions were performed using TomoPy (an open-source software package developed by ANL). ASTRA toolbox was used for the tomographic reconstructions. [57-60] For both micro- and nano- X-ray CT, segmentation was performed in ImageJ, whereas three-dimensional volume rendering was carried in Avizo Fire 8.1 software. Generally, manual threshold values were chosen for additives, MPL, and GDL domains.

2.5. Droplet-detachment studies

Detachment velocity and adhesion-force measurements were carried out on a rotating-stage goniometer (Rame-Hart) with a customized injection system. The detailed drawing of the set-up and a photograph are reported elsewhere [61-62]. The GDL with MPL samples were placed onto the injection port with GDL portion facing up (the channel). The sample cross-section was 3 cm x 3 cm. An Omega PX603 pressure transducer was used to measure liquid pressure. To simulate parallel air flow over the sample, a Lexan flow channel (4 mm x 7 mm) was placed on the GDL with a 10 µL droplet centered in the channel. Dry air flowrate at 20°C was controlled by an Omega FMA-2609A flow controller. The droplet was considered to be detached when its position was outside of its wetting area, and the detachment velocity was defined as the average channel flow at this point based on frame-by-frame video analysis. For the contact angle measurements, 15 µL droplets were placed on top of the GDL or MPL of interest and contact angles were measured with stationary goniometer (Rame-Hart).

2.6. Electron Microscopy

MEA cross-sections were prepared for transmission electron microscopy (TEM) by embedding the MEA in epoxy and microtoming thin slices ~75 nm thick (Leica UCT). The MEA slices were floated in water, captured on a 3 mm Cu grid, and examined in a Hitachi HF3300 TEM operated at 300 kV. MEA cross-sections were also examined in a Hitachi S4800 field emission gun (FEG) scanning electron microscope (SEM) operated at 10 kV.

3. Results

3.1. Cell Performance

Figure 1a shows the polarization curves for the three different MEAs assembled with BC, BL, and BN GDLs at the cathode. As expected, since only the cathode MPL differs, the activation and partially ohmic region (up to ~0.78 V) for all three cells behave similarly; however, at lower potentials, significant differences are observed. At 2 A cm^{-2}, the PEFC with BC shows a low potential of 0.38 V, whereas higher potentials are observed for BL and BN (0.56 and 0.65 V, respectively). More than 200 mV improvement in performance is achieved by replacing the BC GDL with the BN GDL. Figure 1b shows the polarization curves for these MEAs in a HelOx mixture; little performance difference is observed between the MEAs up to 2 A cm^{-2}. Performance measurements clearly highlight the better mass-transport properties that result from the use of MPLs that incorporate hydrophilic additives.

EIS spectra obtained for the same MEAs at high current density (1.4 A cm^{-2}) in air (Figure 1c) and HelOx (Figure 1d) further confirm the observed improvement in mass-transport properties in air for the BL and BN GDLs. The data shown in Figure 1 can be fit (solid lines) using a simple equivalent circuit $R_{HFR}(R_1Q_1)(R_2Q_2)$, where R_{HFR} represents the membrane and contact

resistances, R_1 primarily the kinetic resistance, R_2 primarily the mass transport resistance, and Q_1 and Q_2 are the constant phase elements (distributed capacitances) associated with the electrode processes (Figure 12 from Arisetty et al. [45]). The BL and BN GDLs demonstrate a 50 % and 80 % improvement, respectively, in the mass transport resistance (R_2) over the baseline BC GDL when operated in air at 80 °C, 100 % RH, and 1.4 A cm^{-2}. For the HelOx case the impedance data for all three layers was quite similar. The R_{HFR} for all three cells is approximately the same (~0.04±0.01 Ohm cm^2) at all current densities, indicating similar electrical conductivities and membrane hydration.

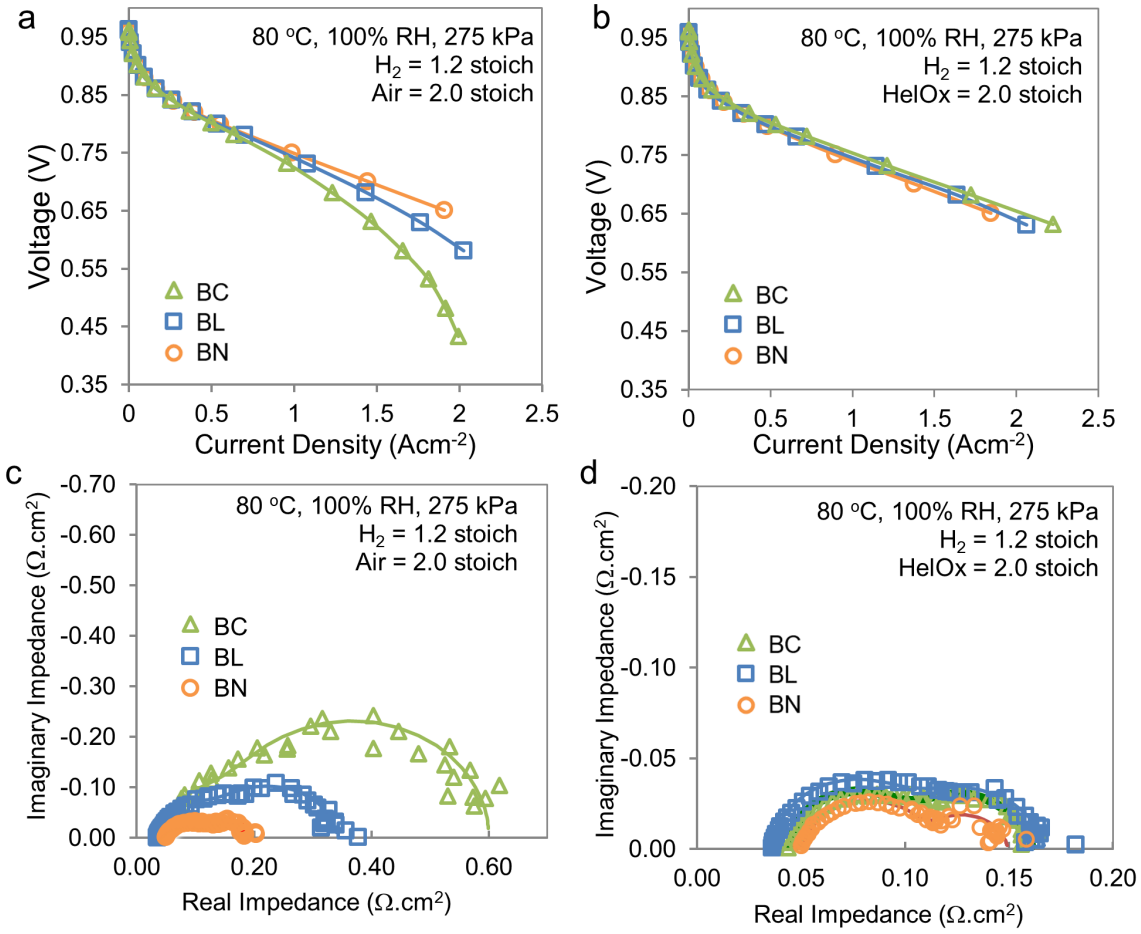

Figure 1. Polarization curves comparing cells with BC, BN, and BL GDLs at 80 °C, 100 % RH, 275 kPa backpressure in a) air at 2 stoichiometric ratio (stoich) and b) HelOx at 2 stoich. EIS

data acquired at 1.4 A cm^{-2}, 100 % RH, and 275 kPa in c) air at 2 stoich and d) HelOx at 2 stoich.

3.2. Durability

To ascertain the overall stability of the MPLs, both *in situ* and *ex situ* (SI) durability studies were conducted. Figure 2 shows the polarization curves at the beginning of test (BOT) and after approximately 300 hours of durability testing (end of test, EOT) using the wet portion of the FCTT durability protocol. Both the BC- and BN-GDL-based MEAs show similar performance decay, which is mainly associated with CCL degradation. These tests were performed using identical MEAs with Pt supported on a highly graphitized carbon (TEC10EA40E) at the cathode to minimize carbon corrosion. These MEAs did exhibit a loss in platinum electrochemically active surface area (ECSA) of ~27 % after 300 hr of testing due to Pt dissolution and re-precipitation under repeated voltage cycling. Both the BC- and BN-GDL-based MEAs show little change in performance under the high-pressure test conditions used other than that associated with Pt ECSA loss. However, the performance of the MEA utilizing the BC GDL demonstrates decay when operated at the lower pressures of the durability cycling test, unlike that of the MEA incorporating the BN GDL. As illustrated in Figure 2b and 2c, BN exhibits virtually no difference in cycling behavior until 600 hr is reached. This stable behavior is in marked contrast to the baseline BC material, where the potential at 1.2 A cm^{-2} drifts to ~0.2 V from its baseline potential of 0.4 V after 389 hr. This drift may be attributed to flooding behavior and poor water management in the cell under transient low pressure conditions. Postmortem analysis of the MEAs with BN GDL for cell operated for 600 hr reveals that the MWCNT domains remain intact (see TEM images in Figures 2e, 2f), although the CCL compacts to some degree (see SEM image in Figure 2d). The performance results combined with microstructural observations demonstrate that the durability of the BN material is superior to that of the BC baseline material. It is speculated that the presence of

hydrophilic channels in the MPL (e.g., the MWCNT domains) potentially mitigate the impacts of hydrophobicity loss in the MPL.

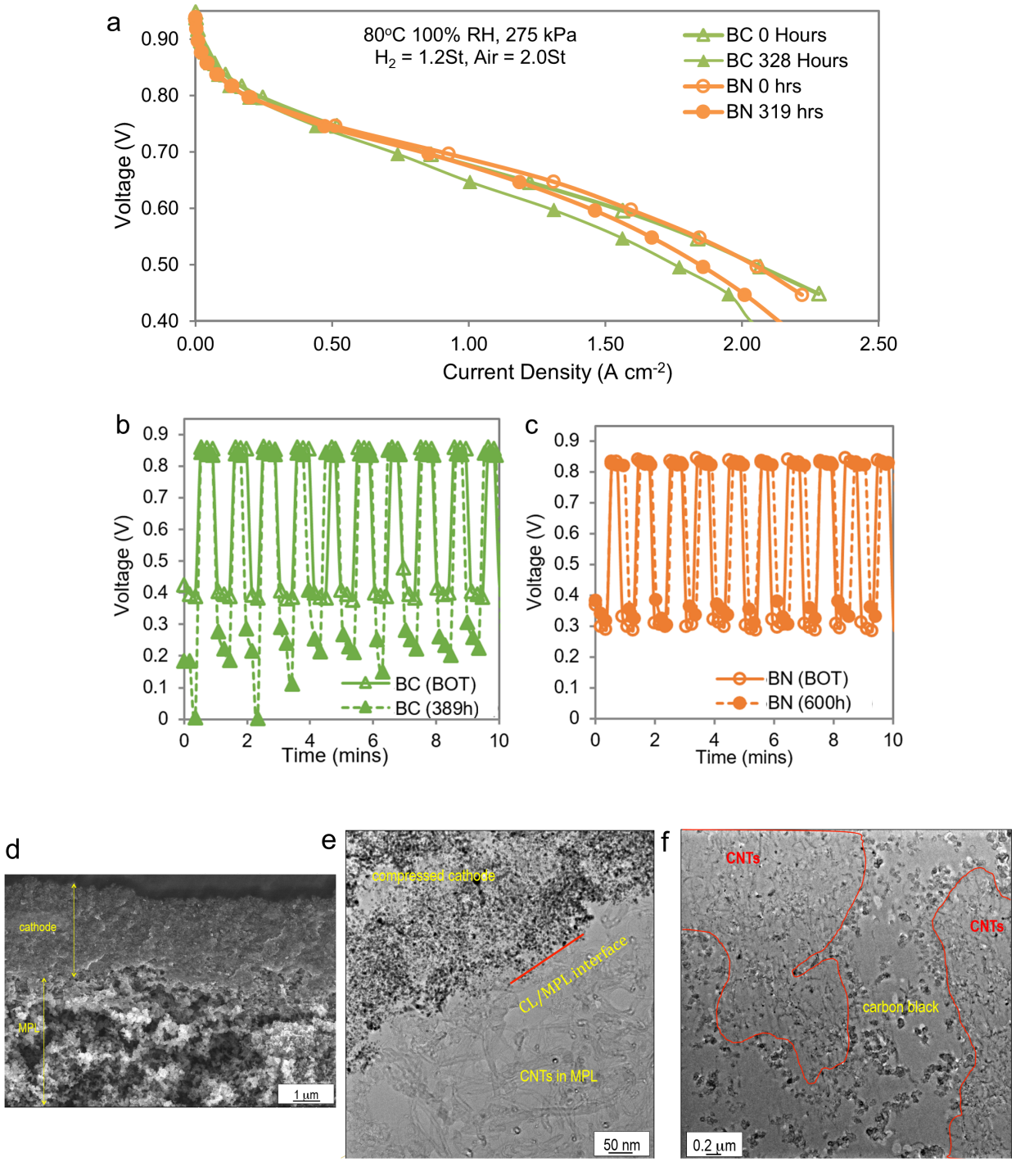

Figure 2. a) Polarization curves for MEAs with BC and BN GDLs at BOT and after 300 hr (EOT) under a durability (cycling) protocol; b) and c) Cycling behavior for the BOT and EOT BC and BN materials, respectively; d) postmortem SEM image showing EOT compacted CCL and porous BN MPL; e) cross-section TEM image of aged CCL and BN MPL interface, where MWCNT domains are clearly observed in the MPL; f) TEM image of aged BN MPL showing domains of carbon black and MWCNTS (porous MWCNT domains outlined in red).

In terms of the BL material, significant degradation was observed, especially in the low frequency resistance (LFR) of the EIS spectrum (see Figure S1). Here, the initial resistance (at 1 A cm^{-2}, 80°C, and 100 % RH) of the BL material is significantly lower than that of the BC baseline; however, after only 36 hours of testing, the BL materials shows a dramatic increase in resistance and the MEA performance is worse than that of the baseline BC material. As shown in Figure S2, this difference is mainly due to dissolution of the aluminosilicate fibers within the MPL and migration of Al and Si from the MPL to the CCL that contaminate the catalyst active sites. Additional *ex-situ* results for durability testing of BC material are presented in Figure S3.

3.3. Operando Properties

To further probe the reason(s) for the polarization changes, water profiles of the three cells were obtained with neutron radiography at three current densities: 0.4 A cm^{-2}, 0.8 A cm^{-2}, and 1.2 A cm^{-2}. Figure 3a shows the polarization curve obtained at NIST for the three MEAs made with BC, BN, and BL GDLs. The difference in performance between the polarization curves in Figure 3 and those shown in Figure 1a is that the polarization data in Figure 3a was collected with zero backpressure and using smaller cell hardware (optimized for neutron imaging) and constant flow conditions, resulting in overall lower current densities, consistent with previous neutron imaging

studies [49, 52]. Nonetheless, similar trends in the mass transport limited region were observed in performance of both 50 cm^2 and 2.5 cm^2 cells, where the cell with the MEA prepared with the BN GDL showed the highest current densities and the lowest resistance. The EIS spectra in Figure 1 were fitted using a standard equivalent circuit where the mass-transport resistance is clearly delineated. However, it is harder to separate quantitatively the charge-transfer and mass-transport resistances in small neutron imaging cells. Still, one can induce that the mass-transport losses are important as the resistance for BN cell is increasingly smaller compared to the other two cells as the current density is increased from 0.4 to 0.8 to 1.2 A cm^{-2}. The onset of the performance deviation was also similar (around 0.8 A cm^{-2}). Similar to the results with large cells, the EIS data in Figure 3 demonstrates similar HFR (high-frequency resistance) for the three MPL/GDL materials but deviations in the LFR at higher current densities.

We further explore the reasons for the performance differences by examining the water thickness profiles, shown in Figure 3 c,d,e. At 0.4 A cm^{-2} (Figure 3c), the BC cell shows the expected profile, where a peak in the water content at 0.7 mm water thickness is observed close to the membrane location of the CCL. The water thickness profile decreases away from the CCL into the MPL and GDL. The cathode GDL shows slightly higher water content than the anode GDL. The water profile for the cell with the MEA prepared with the BL material demonstrates a higher water content in both the CCL and also at both the GDL/bipolar plate interface and/or in the channel. The cell with the BN material shows lower water contents in both cathode and anode compared to the baseline BC cell. At this low current density, the overall water content in the cells is not as high and does not present limitations for oxygen transport, which is in agreement with the EIS data.

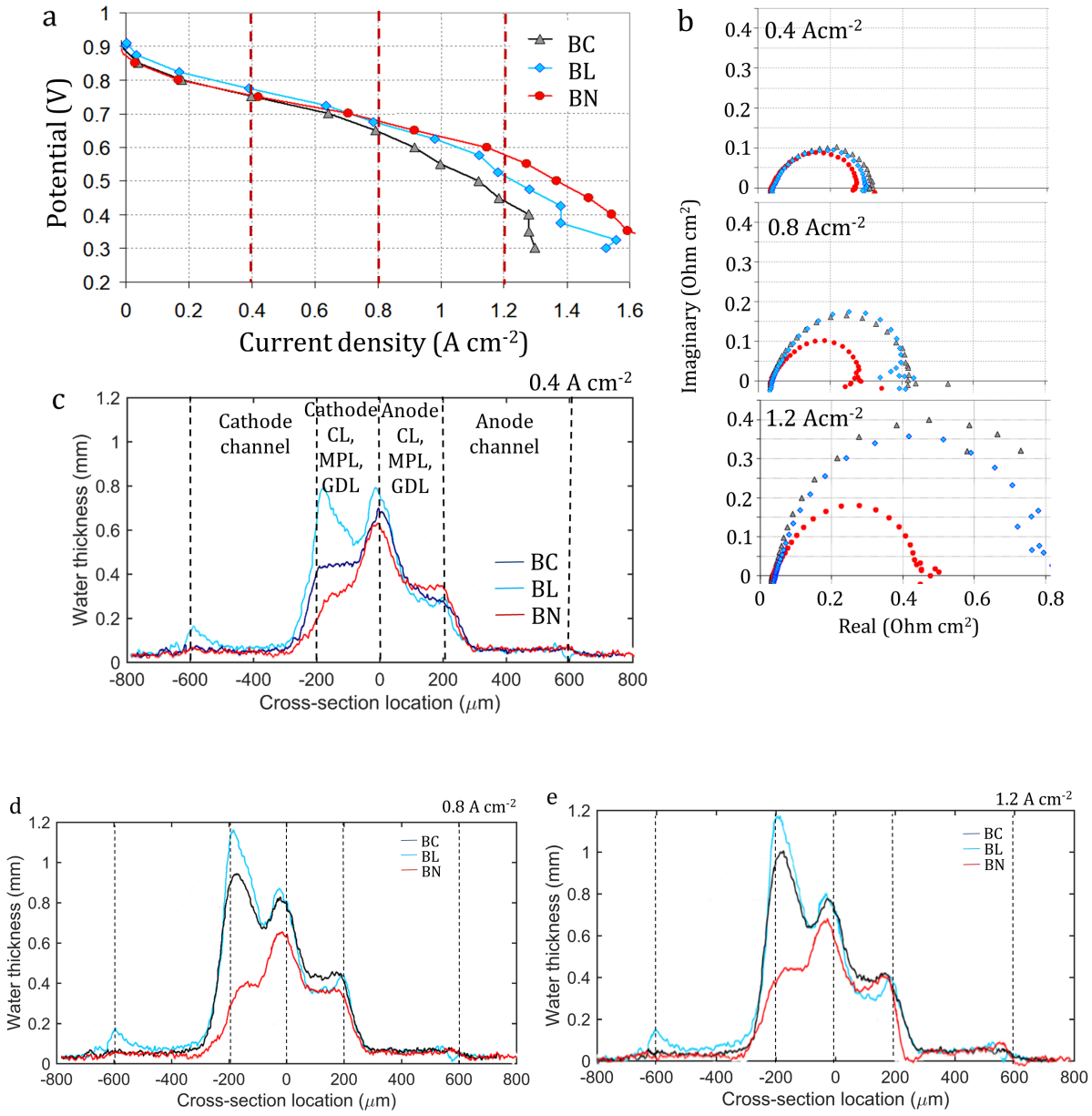

Figure 3. a) BOL polarization curve and three currents under which neutron imaging data was acquired (dotted lines). b) EIS data at three current densities, 0.4, 0.8, 1.2 A cm^{-2} (current densities denoted by dotted lines in (a); c-e) water thickness profiles at the same three current densities in b) acquired at 80 °C, 100 % RH, 100 sccm/200 sccm H_2/air on the anode and cathode, respectively, with zero backpressure.

As the current density is increased from 0.4 A cm^{-2} to 0.8 A cm^{-2}, the overall water content in all cells is increased, especially in the BC and BL cells, most notably in the GDL substrate region. There is very little difference in water profiles recorded at 0.8 A cm^{-2} and 1.2 A cm^{-2}. Both BC and BL materials show similar water profiles, with a water peak at the GDL/flow-field interface, with higher water contents than observed at 0.4 A cm^{-2}. Only the cell with the BN material does not show a peak close to the interface between the GDL and channels and lands (at approx. -200 microns in Figure 3 c,d,e), which might be due to its lower droplet removal velocity (as discussed below). Overall, the BN material shows the lowest water content within the MEA as the current density is increased. Symmetric water profiles with BN material (i.e. similar water in anode and cathode GDLs) indicate balanced water removal through anode and cathode.

We note a few subtleties related to water profiles from neutron imaging. Although the EIS data shows almost identical HFR for all 3 cells, indicating similar levels of membrane hydration, profile plots show different membrane water content. (Also, in separate experiments we measured higher water content in the membrane using much thicker membrane material. [63] [50]). The cathode catalyst layer is likely to have even higher water content than the membrane, however it is located next to the MPL where the water content sharply drops to an extremely low value. Due to the extremely thin fuel cell components (e.g. 18 microns thick membrane), not perfectly straight or flat interfaces between components, and limited resolution of neutron imaging, it is difficult to quantitatively separate the water content at the interfaces and thin components, specifically the membrane, the catalyst layer, and the MPL. It is reasonable to assume that the high water content in the MEA will be averaged with extremely low water content in a standard, highly hydrophobic MPLs adjacent to the MEA. Further, the additive-containing MPLs will have more water compared to almost dry additive-free hydrophobic MPL. One can therefore hypothesize that the high BL water content at the interface between the CCL and the MPL (Figure 3 c,d,e) comes from a combination of

relatively low CCL water and relatively high water content in the MPL due to hydrophilic Al-Si fibers.

3.4. *Ex situ* and *in situ* Properties

In this section, critical *ex situ* properties of the different MPL/GDLs are explored to correlate microstructure and properties with the observed performance differences. Figure 4 shows greyscale X-ray CT tomographs and volume-rendered representations of the GDLs with BC and BN MPLs. The MPL penetrates a large percentage of the void space within the GDL thickness [12] (we refer to this MPL region as the embedded portion of the MPL). Physical properties such as porosity, tortuosity, and pore size distributions for SGL materials were reported previously [8, 37]. The horizontal cross-section chosen for the greyscale tomographs represents a location within the MPL, and from inspection by eye, the differences in the MPL structures between BC and BN appear to be minimal. Both MPLs exhibit cracks, with BC having more cracks within the selected FOV. Figure S4 shows the percentage of crack area for each MPL, with BC having the largest with average of 4 %, which is consistent with the results from an earlier study [37]. The MWCNT domains are about 5 µm in size and with the limited micro-X-ray CT resolution, are not easy to visualize, e.g., the resolution of micro-X-ray CT is 1.3 µm. The BC and BN have increased layer thicknesses of 40-45 µm compared to BA due to the addition of the MPL. However, X-ray CT data shows the average thickness of the entire MPL is ~100 µm, where the MPL thickness is comprised of a free-standing region (outside the fibrous region) and embedded region (embedded between the carbon fibers), indicating that 50-60 µm of MPL is embedded within the GDL. Figure 4e shows the MPL structure, where SEM images and cross-section tomographs show similar morphologies, e.g., dispersed carbon agglomerates coated with PTFE. The BC MPL appears to be quite porous (after thresholding nano-X-ray CT data) with porosity ~50-60 %.

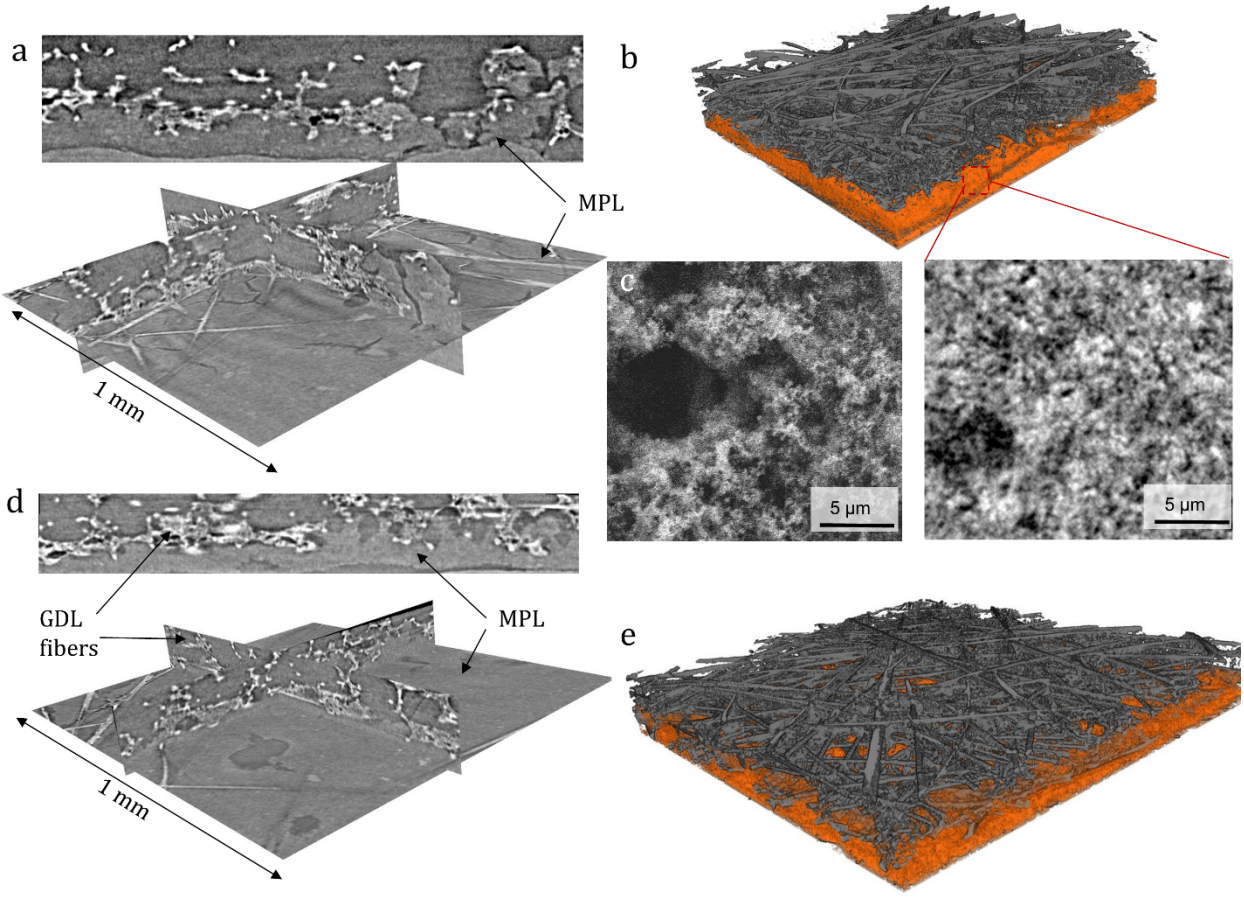

Figure 4. a) Cross-section greyscale tomographs for the baseline BC material and b) the corresponding volume rendered view. c) SEM image of SGL BC (left) and its nano X-ray CT representation (right). d) Cross-section greyscale tomographs of the BN material and e) the corresponding volume rendering.

The nanostructure of the BN material was explored further using nano X-ray CT, the results of which are summarized in Figure 5. The dark dots on the transmission images (Figure 5a and 5b) are the Fe-catalysts of the MWCNTs. The dry sample was imaged two times to ensure sample stability (Figure S5). Figure 5b shows the same sample after deposition of a droplet of water, where it is clear that the water preferentially wets the MWCNT region. Figure 5c and 5d show the

corresponding 3-D cross-sectional tomographs for the dry and wet samples, respectively, where the dry sample demonstrates well-defined MWCNT domains. The MWCNT domains show as blurrier than the teflonized carbon domain because resolution of nano X-ray CT does not allow to resolve individual fibers. Figures S6 and S7 provide additional cross-sections with MWCNT domains highlighted for clarity. Imaging of these MWCNT domains becomes enhanced when in contact with water (Figure 5d), where large water-filled domains and the void space between domains appears. Figure S6 shows detailed analysis of grey-scale values and correlations between the dry (including another dry image location) and wet sample conditions, as well as a volume rendering of the MWCNT domains and proof of the presence of water. It was further observed that the sample was continuously drying during the 20 min. X-ray scan, as water was found at the base of the sample close to the pin, but not much water was found at the tip of the sample where convective drying is most pronounced. Water domains form rather large clusters spanning sizes as large as 600 nm to 800 nm (Figure S6), consistent with the up to 5 μm size of the MWCNT domains. Figure S5 shows an SEM image where the MWCNT domains are clearly evident. In Figure 5d and 6e, water can be clearly distinguished due to the observed change in the greyscale values. The void space is observed via a higher magnification image (Figure 5f). In a previous study, an increase in porosity of about 5 % in BN compared to BC was measured, but no information was given on the void distribution [37]. The nano-CT images show separation of the hydrophilic and hydrophobic domains upon wetting the material with water where water is clearly observed in the MWCNT domains upon wetting.

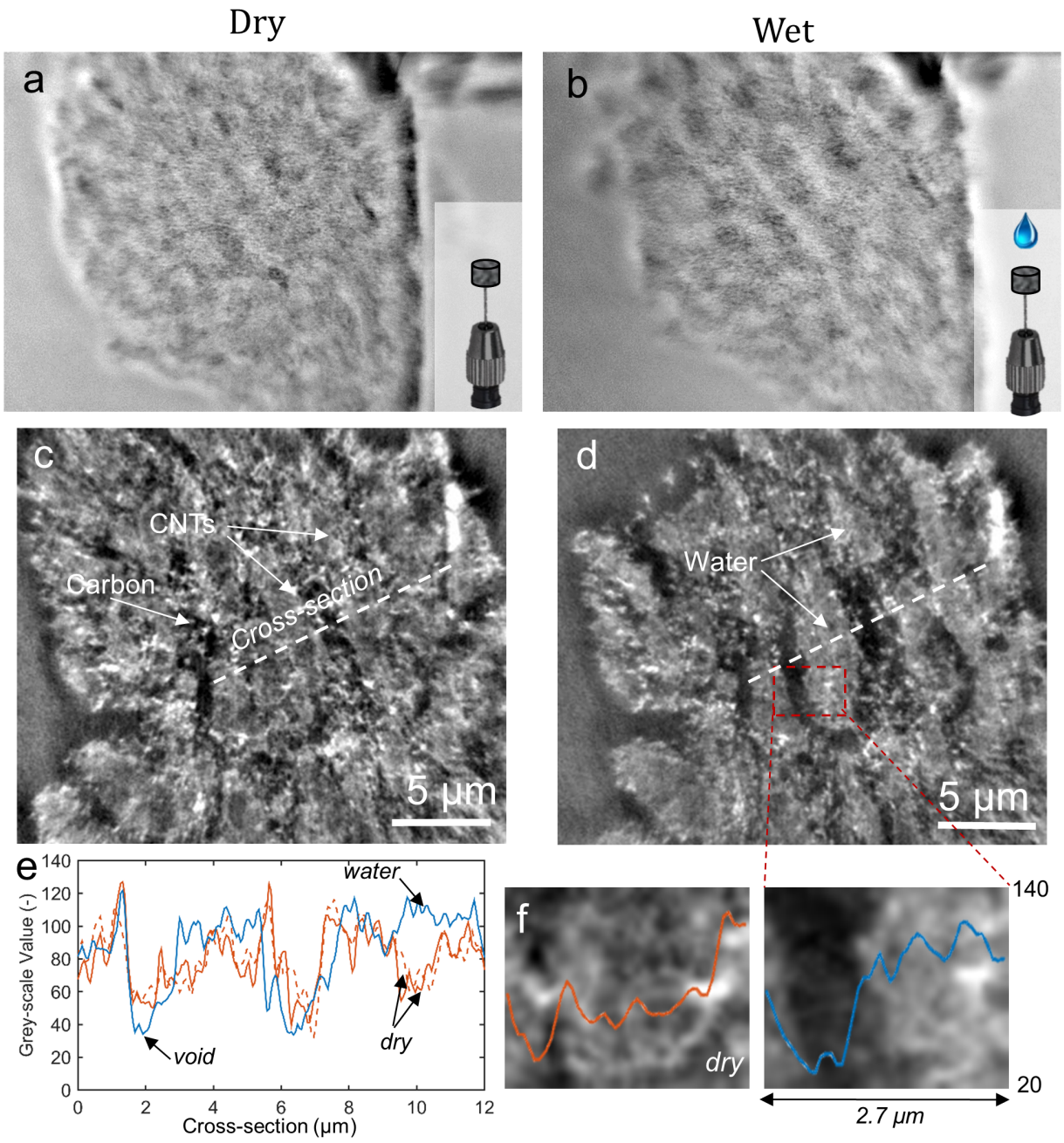

Figure 5. Radiographs of (a) dry and (b) wet samples. Cross-section tomographs of (c) dry and (d) wet BN MPL. e) Greyscale profile along the dashed line within (d), where dry and water samples

are plotted. (f) Higher magnification images of dry and wet samples and corresponding greyscale levels (plotted in (e)).

Figure 6 shows micro X-ray CT results for the BL material, where the aluminosilicate fiber additives are visible (unlike inability to image MWCNTs within the BN material using micro X-ray CT). The fibers are much larger in size than the MWCNT domains with an average length of 29 ± 9 μm. Furthermore, they constitute 2.1 % of the MPL volume. The overall GDL and MPL morphology does not seem to be affected by the presence of the aluminosilicate fibers and remains similar to that observed in the SGL family materials, with the MPL embedded deeply within the GDL. Figure 7 shows SEM (a) and nano-X-ray CT (b-d) images of an aluminosilicate fiber within the BL MPL. The diameter of the fibers is on the order of 5 μm (confirmed by SEM and X-ray CT). The fiber dispersion within the MPL is homogeneous with fibers exhibiting varying lengths and orientations.

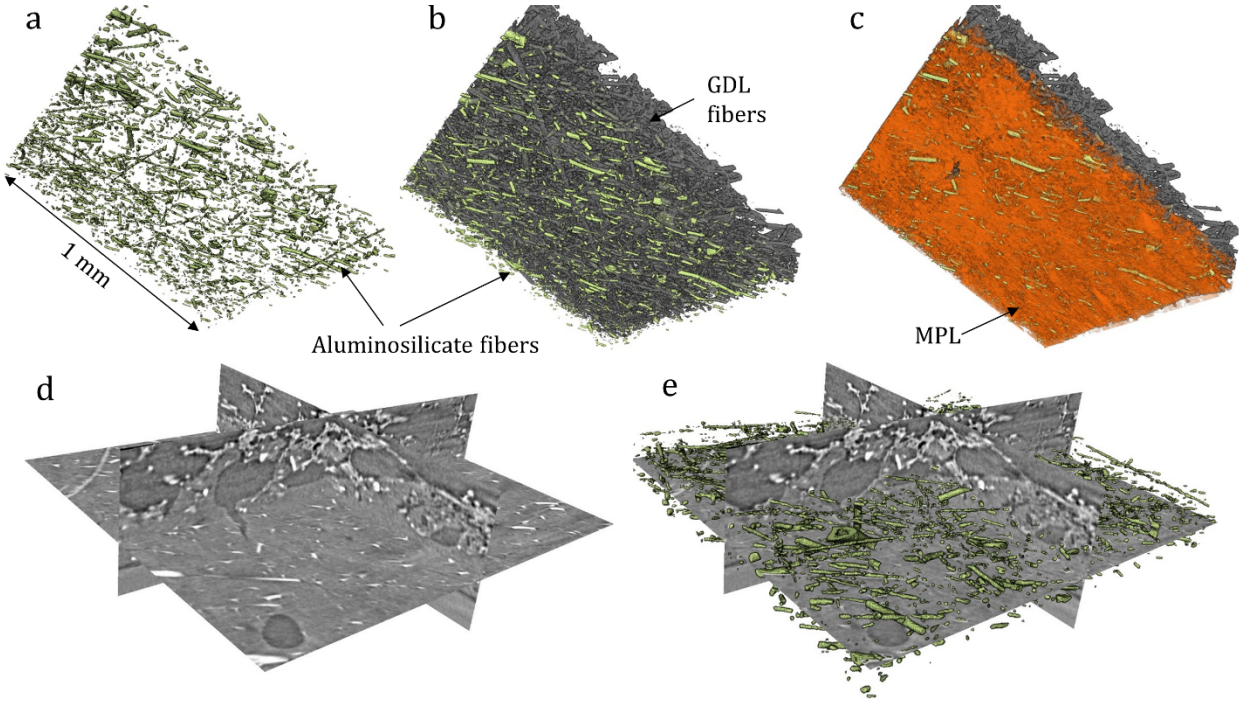

Figure 6. Volume-rendered micro-X-ray CT image stacks for a) aluminosilicate fibers, b) aluminosilicate fibers and GDL fibers, c) MPL and GDL. d) Cross-section greyscale tomographs showing the location of the MPL. e) Same cross-section with aluminosilicate fibers.

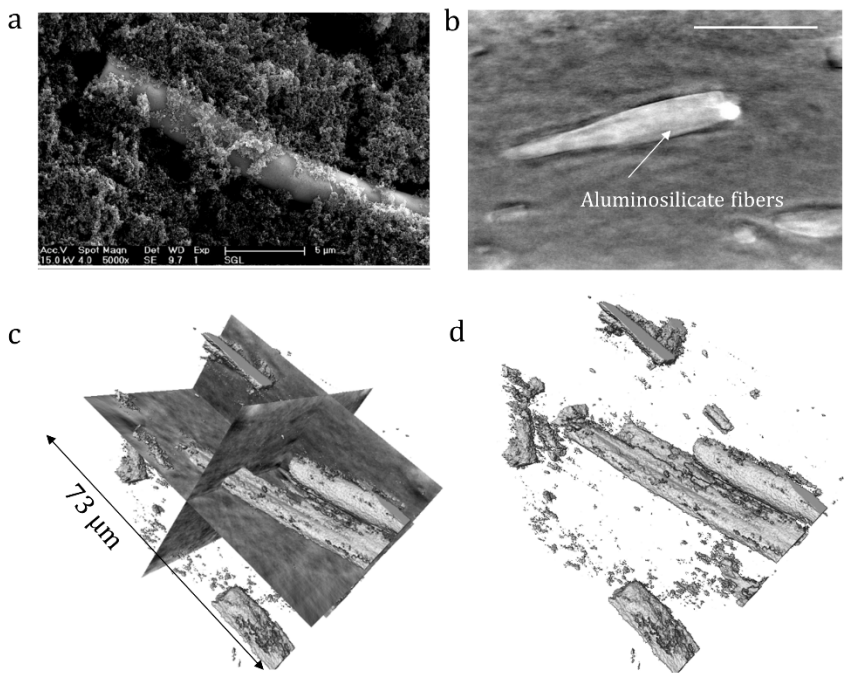

Figure 7. a) SEM image of an aluminosilicate fiber within the BL; b) nano X-ray CT tomograph of fiber and carbon of BL (scale-bar is 50 µm). (c-d) Volume-rendered aluminosilicate fibers within carbon cross-section and with carbon removed.

Figure 8 shows contact angle measurements for the three MPLs studied to explore the wetting properties as well as a film of MWCNTs cast onto a Kapton film. From the external contact angle measurements, which do not probe the internal wettability, no significant variation with contact angles between 162° and 167° were measured, although the BN MPL spontaneously uptakes water as determined from X-ray CT. For the MPLs the droplet heights were 2.4 mm. The film of MWCNTs exhibits hydrophilic behavior with a contact angle of 56°, which is in agreement with the other reported measurements for CNTs[64].

Figure 8e shows the droplet detachment velocity for the BC and BN materials. At all droplet volumes, the detachment velocity is higher for BC material compared to BN, implying that more force is required (or higher gas flowrate) to remove a droplet sitting at the GDL/channel interface for BC compared to BN. The only difference between these materials is their MPL; however, this

difference result in very different water profiles throughout the GDL and it is believed that hydrophilic pathways connectivity results in the observed differences, with BN MPL leading to more connected pathways and less droplet pinning.

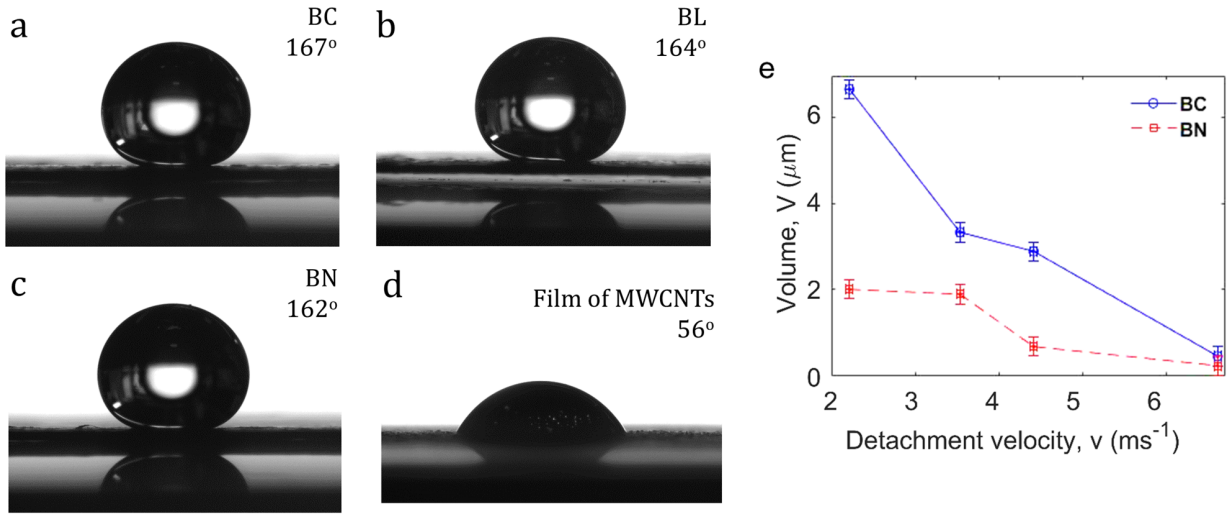

Figure 8. External contact angles measured for a) BC, b) BL, c) BN, and d) a cast film of MWCNTs obtained from the same batch as those in BN. e) Droplet volume as a function of detachment velocity for BC and BN.

4. Discussion

Water management remains an issue for PEFCs at high-current densities, where local water fluxes and water generation are high. From the above *operando* and *ex situ* investigations, it is clear that the BN and BL MPLs result in different water management schemes than traditional hydrophobic BC MPLs by providing hydrophilic pathways (see Figure 8) created by additives that help remove water from the cathode catalyst layer as shown explicitly by *in situ* nano X-ray CT imaging. The improved performance observed with BN MPL in particular is primarily due to several factors:

1) Cell with BN MPL on the cathode shows reduced water content within all the PEFC components, as observed by neutron radiography. From the microstructural observations, this enhanced water removal behavior is likely due to the presence of the hydrophilic MWCNT domains that wick water from the catalyst layer. Furthermore, from droplet removal velocity studies, the BN shows a lower detachment velocity compared to the BC, indicating that the effects of the MPL propagate into the structure of the GDL. The performance enhancement induced by BL was not as obvious, but it appears that the aluminosilicate fibers serve a similar purpose to that of the MWCNT domains, with more water removed in liquid form from CCL into the GDL fiber substrate.
2) The cell with BN MPL shows higher durability during a drive-cycle protocol, with no indication of flooding, whereas BC exhibits potential drift due to local flooding. Cell with the BL MPL was not as stable during the durability study due to elemental dissolution of the aluminosilicate fibers, the elements of which migrated into the catalyst layer.
3) All three GDLs showed similar performance under HelOx operation, whereas under air the cell performance deviated for the three GDLs at high current densities. Fitting of the EIS data confirmed that under air operation the GDLs with additives showed significantly improved mass transport. This behavior is perhaps due to segregation of hydrophilic and hydrophobic domains for the BL and BN materials, resulting in lower overall water contents in the catalyst layer and improved reactant accessibility. Furthermore, the extra voids that are formed in the BN during wetting can help oxygen transport even when a significant amount of water is present, as the MWCNT domains are spatially separated from the highly hydrophobic PTFE impregnated carbon regions in the MPL.

5. Summary

Polymer-electrolyte fuel cells (PEFCs) experience water-management issues at high current densities, where conventional hydrophobic MPLs serve as high capillary-pressure barriers. These MPLs ensure a high water content within the catalyst layers to provide good membrane hydration; however, such a barrier results in possible factor for flooding of the catalyst layer. Engineering novel MPLs can enable higher PEFC performance and minimize catalyst-layer flooding. In the present article, two additive-containing MPLs - SGL 25 BL and SGL 25 BN - were explored using a systematic series of *in-situ*, *operando*, and *ex-situ* techniques to understand the performance changes engendered by these MPLs. From these studies, it is clear that incorporation of the additives result in different water management behavior by providing hydrophilic pathways that help remove water from the cathode catalyst layer, as shown by *in situ* nano-X-ray computed tomography. The improved water management and less flooding results in enhanced performance in terms of polarization owing to less water in the cathode catalyst layer and easier water movement out of the cell, in agreement with the various cell measurements and diagnostics. More efficient water management also results in increased durability related to water management during corrosion testing for SGL 25 BN. Although the SGL 25 BL showed a promising concept when water management is concerned (hydrophilic pathways for water removal through predominantly hydrophobic MPL), aluminosilicate fibers also led to durability issues related to catalyst poisoning (Al and Si dissolution and migration into catalyst layer). Overall, engineered MPLs with hydrophilic additives or structures (e.g., MWCNTs) are a promising route towards optimizing PEFC performance and durability due to their ability to control and transport water and make hydraulic connections throughout the cell components.

ASSOCIATED CONTENT

Supporting Information Available: Additional EIS spectra before and after aging test for, cross-sectional SEMs and elemental mapping, nano X-ray CT additional data

Acknowledgements

We would like thank Peter Wilde and Ruediger-Bernd Schweiss from SGL for providing the MPLs and GDLs used in this study. I.V.Z. would like to acknowledge support from the National Science Foundation under CBET Award 1605159. This research used resources of the Advanced Photon Source, a U.S. Department of Energy (DOE) Office of Science User Facility operated for the U.S. DOE Office of Science by Argonne National Laboratory under Contract No. DE-AC02-06CH11357. Microscopy conducted as part of a user proposal at ORNL's Center for Nanophase Materials Sciences, which is a U.S. DOE Office of Science User Facility. Research was supported by the Fuel Cell Technologies, Office Energy Efficiency and Renewable Energy, U.S. DOE, and was conducted through the FC-PAD Consortium. The authors would like to acknowledge the support of the technology development managers Nancy Garland, Greg Kleen, and Dimitrios Papageorgopoulos. This work was also supported by the U.S. Department of Commerce, the NIST Ionizing Radiation Division, the Director's Office of NIST, the NIST Center for Neutron Research, and the Department of Energy through interagency agreement no. DE-AI01-01EE50660.

References

1. Kongkanand, A.; Mathias, M. F., The Priority and Challenge of High-Power Performance of Low-Platinum Proton-Exchange Membrane Fuel Cells. *The Journal of Physical Chemistry Letters* **2016,** *7* (7), 1127-1137.
2. Steinbach, A. J.; Allen, J. S.; Borup, R. L.; Hussey, D. S.; Jacobson, D. L.; Komlev, A.; Kwong, A.; MacDonald, J.; Mukundan, R.; Pejsa, M. J.; Roos, M.; Santamaria, A. D.; Sieracki, J. M.; Spernjak, D.; Zenyuk, I. V.; Weber, A. Z., Anode-Design Strategies for Improved Performance of Polymer-Electrolyte Fuel Cells with Ultra-Thin Electrodes. *Joule* **2018**.
3. Shum, A. D.; Parkinson, D. Y.; Xiao, X.; Weber, A. Z.; Burheim, O. S.; Zenyuk, I. V., Investigating Phase-Change-Induced Flow in Gas Diffusion Layers in Fuel Cells with X-ray Computed Tomography. *Electrochimica Acta* **2017,** *256*, 279-290.
4. Weber, A. Z.; Borup, R. L.; Darling, R. M.; Das, P. K.; Dursch, T. J.; Gu, W.; Harvey, D.; Kusoglu, A.; Litster, S.; Mench, M. M.; Mukundan, R.; Owejan, J. P.; Pharoah, J. G.; Secanell, M.; Zenyuk, I. V., A Critical Review of Modeling Transport Phenomena in Polymer-Electrolyte Fuel Cells. *J Electrochem Soc* **2014,** *161* (12), F1254-F1299.
5. Weber, A. Z.; Hickner, M. A., Modeling and high-resolution-imaging studies of water-content profiles in a polymer-electrolyte-fuel-cell membrane-electrode assembly. *Electrochimica Acta* **2008,** *53* (26), 7668-7674.
6. Weber, A. Z.; Newman, J., Coupled Thermal and Water Management in Polymer Electrolyte Fuel Cells. *J Electrochem Soc* **2006,** *153* (12), A2205.
7. Kusoglu, A.; Dursch, T. J.; Weber, A. Z., Nanostructure/Swelling Relationships of Bulk and Thin-Film PFSA Ionomers. *Advanced Functional Materials* **2016,** *26* (27), 4961-4975.
8. Zenyuk, I. V.; Parkinson, D. Y.; Connolly, L. G.; Weber, A. Z., Gas-diffusion-layer structural properties under compression via X-ray tomography. *Journal of Power Sources* **2016,** *328*, 364-376.
9. Zenyuk, I. V.; Kumbur, E. C.; Litster, S., Deterministic contact mechanics model applied to electrode interfaces in polymer electrolyte fuel cells and interfacial water accumulation. *Journal of Power Sources* **2013,** *241*, 379-387.
10. Zenyuk, I. V.; Taspinar, R.; Kalidindi, A. R.; Kumbur, E. C.; Litster, S., Computational and Experimental Analysis of Water Transport at Component Interfaces in Polymer Electrolyte Fuel Cells. *J Electrochem Soc* **2014,** *161* (11), F3091-F3103.
11. Qi, Z.; Kaufman, A., Enhancement of PEM fuel cell performance by steaming or boiling the electrode. *Journal of Power Sources* **2002,** *109* (1), 227-229.
12. Atkinson, R. W., Garsany, Y., Gould, B.D., Swider-Lyons, K.E., Zenyuk, I.V., The role of compressive stress on gas diffuion media morphology and fuel cell performance. *ACS Applied Energy Materials* **2017,** *1* (1).
13. Spernjak, D.; Prasad, A. K.; Advani, S. G., Experimental investigation of liquid water formation and transport in a transparent single-serpentine PEM fuel cell. *Journal of Power Sources* **2007,** *170* (2), 334-344.
14. Zenyuk, I. V.; Lamibrac, A.; Eller, J. J.; Parkinson, D. Y.; Marone, F.; Büchi, F. N.; Weber, A. Z., Investigating Evaporation in Gas Diffusion Layers for Fuel Cells with X-ray Computed Tomography. *The Journal of Physical Chemistry C* **2016**.
15. Bock, R.; Shum, A.; Khoza, T.; Seland, F.; Hussain, N.; Zenyuk, I. V.; Burheim, O. S., Experimental Study of Thermal Conductivity and Compression Measurements of the GDL-MPL Interfacial Composite Region. *ECS Transactions* **2016,** *75* (14), 189-199.
16. Burheim, O. S.; Su, H.; Pasupathi, S.; Pharoah, J. G.; Pollet, B. G., Thermal conductivity and temperature profiles of the micro porous layers used for the polymer electrolyte membrane fuel cell. *International Journal of Hydrogen Energy* **2013,** *38* (20), 8437-8447.

17. Owejan, J. P.; Owejan, J. E.; Gu, W.; Trabold, T. A.; Tighe, T. W.; Mathias, M. F., Water Transport Mechanisms in PEMFC Gas Diffusion Layers. *J Electrochem Soc* **2010,** *157* (10), B1456-B1464.
18. Karan, K.; Atiyeh, H.; Phoenix, A.; Halliop, E.; Pharoah, J.; Peppley, B., An Experimental Investigation of Water Transport in PEMFCs: The Role of Microporous Layers. *Electrochemical and Solid-State Letters* **2007,** *10* (2), B34-B38.
19. Spernjak, D.; Fairweather, J.; Mukundan, R.; Rockward, T.; Borup, R. L., Influence of the microporous layer on carbon corrosion in the catalyst layer of a polymer electrolyte membrane fuel cell. *Journal of Power Sources* **2012,** *214*, 386-398.
20. Zhou, J.; Shukla, S.; Putz, A.; Secanell, M., Analysis of the role of the microporous layer in improving polymer electrolyte fuel cell performance. *Electrochimica Acta* **2018,** *268*, 366-382.
21. Gallo Stampino, P.; Cristiani, C.; Dotelli, G.; Omati, L.; Zampori, L.; Pelosato, R.; Guilizzoni, M., Effect of different substrates, inks composition and rheology on coating deposition of microporous layer (MPL) for PEM-FCs. *Catalysis Today* **2009,** *147*, S30-S35.
22. Park, S.; Lee, J.-W.; Popov, B. N., Effect of PTFE content in microporous layer on water management in PEM fuel cells. *Journal of Power Sources* **2008,** *177* (2), 457-463.
23. Kannan, A. M.; Menghal, A.; Barsukov, I. V., Gas diffusion layer using a new type of graphitized nano-carbon PUREBLACK® for proton exchange membrane fuel cells. *Electrochemistry Communications* **2006,** *8* (5), 887-891.
24. Schweiss, R., Benefits of Membrane Electrode Assemblies with Asymmetrical GDL Configurations for PEM Fuel Cells. *Fuel Cells* **2016,** *16* (1), 100-106.
25. Simon, C.; Kartouzian, D.; Müller, D.; Wilhelm, F.; Gasteiger, H. A., Impact of Microporous Layer Pore Properties on Liquid Water Transport in PEM Fuel Cells: Carbon Black Type and Perforation. *J Electrochem Soc* **2017,** *164* (14), F1697-F1711.
26. Mukundan, R.; Davey, J.; Fairweather, J. D.; Spernjak, D.; Spendelow, J. S.; Hussey, D. S.; Jacobson, D.; Wilde, P.; Schweiss, R.; Borup, R. L., Effect of Hydrophilic Treatment of Microporous Layer on Fuel Cell Performance. *ECS Transactions* **2010,** *33* (1), 1109-1114.
27. Hou, S.; Su, H.; Zou, H.; Dang, D.; Song, H.; Li, X.; Liao, S., Enhanced low-humidity performance in a proton exchange membrane fuel cell by the insertion of microcrystalline cellulose between the gas diffusion layer and the anode catalyst layer. *International Journal of Hydrogen Energy* **2015,** *40* (45), 15613-15621.
28. Chun, J. H.; Park, K. T.; Jo, D. H.; Lee, J. Y.; Kim, S. G.; Park, S. H.; Lee, E. S.; Jyoung, J.-Y.; Kim, S. H., Development of a novel hydrophobic/hydrophilic double micro porous layer for use in a cathode gas diffusion layer in PEMFC. *International Journal of Hydrogen Energy* **2011,** *36* (14), 8422-8428.
29. Kitahara, T.; Nakajima, H.; Inamoto, M.; Shinto, K., Triple microporous layer coated gas diffusion layer for performance enhancement of polymer electrolyte fuel cells under both low and high humidity conditions. *Journal of Power Sources* **2014,** *248*, 1256-1263.
30. Kitahara, T.; Nakajima, H.; Inamoto, M.; Morishita, M., Novel hydrophilic and hydrophobic double microporous layer coated gas diffusion layer to enhance performance of polymer electrolyte fuel cells under both low and high humidity. *Journal of Power Sources* **2013,** *234*, 129-138.
31. Schweiss, R.; Steeb, M.; Wilde, P. M.; Schubert, T., Enhancement of proton exchange membrane fuel cell performance by doping microporous layers of gas diffusion layers with multiwall carbon nanotubes. *Journal of Power Sources* **2012,** *220*, 79-83.
32. Lin, S.-Y.; Chang, M.-H., Effect of microporous layer composed of carbon nanotube and acetylene black on polymer electrolyte membrane fuel cell performance. *International Journal of Hydrogen Energy* **2015,** *40* (24), 7879-7885.
33. Jung, G.-B.; Tzeng, W.-J.; Jao, T.-C.; Liu, Y.-H.; Yeh, C.-C., Investigation of porous carbon and carbon nanotube layer for proton exchange membrane fuel cells. *Applied Energy* **2013,** *101*, 457-464.

34. Kitahara, T.; Nakajima, H.; Okamura, K., Gas diffusion layers coated with a microporous layer containing hydrophilic carbon nanotubes for performance enhancement of polymer electrolyte fuel cells under both low and high humidity conditions. *Journal of Power Sources* **2015,** *283*, 115-124.
35. Tanuma, T.; Kinoshita, S., Impact of Cathode Fabrication on Fuel Cell Performance. *J Electrochem Soc* **2014,** *161* (1), F94-F98.
36. Tanuma, T.; Kawamoto, M.; Kinoshita, S., Effect of Properties of Hydrophilic Microporous Layer (MPL) on PEFC Performance. *J Electrochem Soc* **2017,** *164* (6), F499-F503.
37. Lee, J.; Banerjee, R.; George, M. G.; Muirhead, D.; Shrestha, P.; Liu, H.; Ge, N.; Chevalier, S.; Bazylak, A., Multiwall Carbon Nanotube-Based Microporous Layers for Polymer Electrolyte Membrane Fuel Cells. *J Electrochem Soc* **2017,** *164* (12), F1149-F1157.
38. Aoyama, Y.; Tabe, Y.; Nozaki, R.; Suzuki, K.; Chikahisa, T.; Tanuma, T., Analysis of Water Transport inside Hydrophilic Carbon Fiber Micro-Porous Layers with High-Performance Operation in PEFC. *J Electrochem Soc* **2018,** *165* (7), F484-F491.
39. Ahn, M.; Cho, Y.-H.; Cho, Y.-H.; Kim, J.; Jung, N.; Sung, Y.-E., Influence of hydrophilicity in micro-porous layer for polymer electrolyte membrane fuel cells. *Electrochimica Acta* **2011,** *56* (5), 2450-2457.
40. Weber, A. Z., Improved modeling and understanding of diffusion-media wettability on polymer-electrolyte-fuel-cell performance. *Journal of Power Sources* **2010,** *195* (16), 5292-5304.
41. Kim, S.; Mench, M. M., Physical degradation of membrane electrode assemblies undergoing freeze/thaw cycling: Micro-structure effects. *Journal of Power Sources* **2007,** *174* (1), 206-220.
42. Ramasamy, R. P.; Kumbur, E. C.; Mench, M. M.; Liu, W.; Moore, D.; Murthy, M., Investigation of macro- and micro-porous layer interaction in polymer electrolyte fuel cells. *International Journal of Hydrogen Energy* **2008,** *33* (13), 3351-3367.
43. Certain trade names and company products are mentioned in the text or identified in an illustration in order to adequately specify the experimental procedure and equipment used. In no case does such identification imply recommendation or endorsement by the National Institute of Standards and Technology, nor does it imply that the products are necessarily the best available for the purpose.
44. Gharibi, H.; Javaheri, M.; Mirzaie, R. A., The synergy between multi-wall carbon nanotubes and Vulcan XC72R in microporous layers. *International Journal of Hydrogen Energy* **2010,** *35* (17), 9241-9251.
45. Arisetty, S.; Wang, X.; Ahluwalia, R. K.; Mukundan, R.; Borup, R.; Davey, J.; Langlois, D.; Gambini, F.; Polevaya, O.; Blanchet, S., Catalyst Durability in PEM Fuel Cells with Low Platinum Loading. *Journal of The Electrochemical Society* **2012,** *159* (5), B455-B462.
46. Friedrich, K. A., Schulze, M. In *Overview of the FP7 Project DECODE Results and Recommendations*, 2nd International Workshop on Degradation Issues of Fuel Cells, 2011.
47. Mukundan, R.; Davey, J. R.; Rau, K.; Langlois, D. A.; Spernjak, D.; Fairweather, J. D.; Artyushkova, K.; Schweiss, R.; Borup, R. L., Degradation of Gas Diffusion Layers in PEM Fuel Cells during Drive Cycle Operation. *ECS Transactions* **2013,** *58* (1), 919-926.
48. Energy, C. F. C.-D. o. Chapter 3.4 Fuel Cells- Department of Energy. https://energy.gov/sites/prod/files/2017/05/f34/fcto_myrdd_fuel_cells.pdf.
49. Hussey, D. S.; Spernjak, D.; Weber, A. Z.; Mukundan, R.; Fairweather, J.; Brosha, E. L.; Davey, J.; Spendelow, J. S.; Jacobson, D. L.; Borup, R. L., Accurate measurement of the through-plane water content of proton-exchange membranes using neutron radiography. *Journal of Applied Physics* **2012,** *112* (10), 104906.
50. Mukundan, R.; Borup, R. L., Visualising Liquid Water in PEM Fuel Cells Using Neutron Imaging. *Fuel Cells* **2009,** *9* (5), 499-505.
51. Siegmund, O.; Tremsin, A.; Vallerga, J.; McPhate, J., Microchannel plate cross-strip detectors with high spatial and temporal resolution. *Nuclear Instruments and Methods in Physics Research Section A: Accelerators, Spectrometers, Detectors and Associated Equipment* **2009,** *610* (1), 118-122.

52. Mukundan, R.; Davey, J. R.; Rockward, T.; Spendelow, J. S.; Pivovar, B.; Hussey, D. S.; Jacobson, D. L.; Arif, M.; Borup, R., Imaging of Water Profiles in PEM Fuel Cells Using Neutron Radiography: Effect of Operating Conditions and GDL Composition. *ECS Transactions* **2007,** *11* (1), 411-422.
53. Fairweather, J. D.; Spernjak, D.; Weber, A. Z.; Harvey, D.; Wessel, S.; Hussey, D. S.; Jacobson, D. L.; Artyushkova, K.; Mukundan, R.; Borup, R. L., Effects of Cathode Corrosion on Through-Plane Water Transport in Proton Exchange Membrane Fuel Cells. *J Electrochem Soc* **2013,** *160* (9), F980-F993.
54. Schneider, C. A.; Rasband, W. S.; Eliceiri, K. W., NIH Image to ImageJ: 25 years of image analysis. *Nature Methods* **2012,** *9*, 671.
55. Abramoff, M.; Magalhães, P. J.; Ram, S. J., Image processing with ImageJ. *Biophotonics international* **2004,** *11* (7), 36-42.
56. Groso, A.; Abela, R.; Stampanoni, M., Implementation of a fast method for high resolutionphase contrast tomography. *Opt. Express* **2006,** *14* (18), 8103-8110.
57. Gürsoy, D.; De Carlo, F.; Xiao, X.; Jacobsen, C., TomoPy: a framework for the analysis of synchrotron tomographic data. *Journal of Synchrotron Radiation* **2014,** *21* (Pt 5), 1188-1193.
58. Pelt, D. M.; Gürsoy, D.; Palenstijn, W. J.; Sijbers, J.; De Carlo, F.; Batenburg, K. J., Integration of TomoPy and the ASTRA toolbox for advanced processing and reconstruction of tomographic synchrotron data. *Journal of synchrotron radiation* **2016,** *23* (3), 842-849.
59. De Carlo, F.; Gürsoy, D.; Marone, F.; Rivers, M.; Parkinson, D. Y.; Khan, F.; Schwarz, N.; Vine, D. J.; Vogt, S.; Gleber, S.-C., Scientific data exchange: a schema for HDF5-based storage of raw and analyzed data. *Journal of synchrotron radiation* **2014,** *21* (6), 1224-1230.
60. De Andrade, V.; Deriy, A.; Wojcik, M. J.; Gürsoy, D.; Shu, D.; Fezzaa, K.; De Carlo, F., Nanoscale 3D imaging at the advanced photon source.
61. Santamaria, A. D.; Das, P. K.; MacDonald, J. C.; Weber, A. Z., Liquid-Water Interactions with Gas-Diffusion-Layer Surfaces. *J Electrochem Soc* **2014,** *161* (12), F1184-F1193.
62. Das, P. K.; Grippin, A.; Kwong, A.; Weber, A. Z., Liquid-water-droplet adhesion-force measurements on fresh and aged fuel-cell gas-diffusion layers. *J Electrochem Soc* **2012,** *159* (5), B489-B496.
63. Spernjak, D.; Mukherjee, P. P.; Mukundan, R.; Davey, J.; Hussey, D. S.; Jacobson, D.; Borup, R. L., Measurement of water content in polymer electrolyte membranes using high resolution neutron imaging. *Ecs Transactions* **2010,** *33* (1), 1451-1456.
64. Pavese, M.; Musso, S.; Bianco, S.; Giorcelli, M.; Pugno, N., An analysis of carbon nanotube structure wettability before and after oxidation treatment. *Journal of Physics: Condensed Matter* **2008,** *20* (47), 474206.